# Novel Ultrathin Nanoflake Assembled Porous MnO$_2$/Carbon Strip Microspheres for Superior Pseudocapacitors

Guiling Wang,[†,§] Yuwen Liu,[†,§] Guangjie Shao,*[,†,‡,§] Lingxue Kong,[‡] and Weimin Gao*[,‡]

[†]State Key Laboratory of Metastable Materials Science and Technology, Yanshan University, Qinhuangdao 066004, China
[‡]Institute for Frontier Materials, Deakin University, Geelong, Victoria 3220, Australia
[§]College of Environmental and Chemical Engineering, Yanshan University, Qinhuangdao 066004, China

Ⓢ *Supporting Information*

ABSTRACT: A novel hierarchical MnO$_2$/carbon strip (MnO$_2$/C) microsphere is synthesized via galvanostatic charge−discharge of a MnO@C matrix precursor where the carbon is from a low-cost citric acid. This hierarchical structure is composed of manganese oxides nanoflakes and inlaid carbon strips. The ultrathin nanoflakes assemble to form porous microspheres with a rippled surface superstructure. Due to its improved conductivity and remarkable increased phase contact area, this novel structure exhibits an excellent electrochemical performance with a specific capacitance of 485.6 F g^{-1} at a current density of 0.5 A g^{-1} and an area capacitance as high as 4.23 F cm^{-2} at a mass loading of 8.7 mg cm^{-2}. It also shows an excellent cycling stability with 88.9% capacity retention after 1000 cycles. It is speculated that the present low-cost novel hierarchical porous microspheres can serve as a promising electrode material for pseudocapacitors.

KEYWORDS: *Carbon sources, Manganese oxides, Pseudocapacitor, Galvanostatic charge−discharge, Porous*
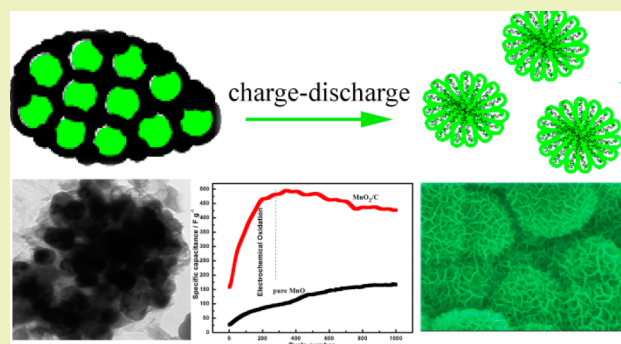
■ INTRODUCTION

Manganese oxides are considered to be a promising material for pseudocapacitors because of their high theoretical specific capacitance of up to 1370 F g^{-1} as the oxidation state of Mn ion changes from 4+ to 3+ over a potential window of 0.8 V,[1] their low cost imparted by the natural abundance, and their environmentally friendliness. The practical capacitive behavior of MnO$_2$ materials is, however, far from the theoretical value due to their poor electrical conductivity (approximately 10^{-5} to 10^{-6} S cm^{-1}) and mechanical instability.[2−4] To overcome this shortage, many efforts have been made, to introduce conductive materials, such as carbonaceous materials,[5−9] metals,[10−13] conducting polymers,[14−16] and metal oxides.[6,10,17] Among of these conductive materials, carbon is generally considered to be one of the most promising candidates for their high electrical conductivity, large surface area, and good mechanical stability. It has been demonstrated that these carbon-based materials can lead to an increase in specific capacitance. For example, Mn$_3$O$_4$/amorphous-carbon nanoparticles synthesized via a green chemistry route, exhibited a capacitance of up to 522 F g^{-1} at a specific current density of 1 A g^{-1}.[18] CNT sheet/MnO$_x$ composites were synthesized by electrodepositing MnO$_x$ on CNT multisheets. When the thickness of MnO$_x$ is ~70 nm, the specific capacitance of the composites has a high value of 1250 F g^{-1}. After the thickness increased to 800 nm, the capacitance is only 190 F g^{-1}.[19] Note that the most notable enhancement in

the specific capacitance has been obtained from the samples having a manganese oxide content of no more than 70% and at an active-material loading density of less than 1 mg cm^{-2}.[20−23]

Both the low manganese oxide content and the low active materials loading will significantly affect the overall energy density per area of the electrodes. In recent years, many researchers have worked on the technique of increasing the utilization of active materials and loading of manganese oxide.[24−27] Lei et al.[28] prepared a supercapacitor electrode composed of graphenes and MnO$_2$-coated carbon naontubes between the graphenes. A maximum specific capacitance of 193 F g^{-1} was achieved and a capacitance retention of 70% after 1300 cycles was observed at a mass loading of 4 mg cm^{-2}. To enhance the electrochemically active surface area of MnO$_2$, growing ultrathin MnO$_2$ nanofibers on graphitic hollow carbon spheres was conducted by refluxing the carbon spheres in a KMnO$_4$ aqueous solution, yielding a sample with an MnO$_2$ content of 64%, which produced a specific capacitance of 190 F g^{-1} at a mass loading of 5.0 mg cm^{-2}.[29] A three-dimensional graphene network loaded with MnO$_2$ was prepared by electrodeposition, which yielded an area capacitance of 1.42 F cm^{-2} at an MnO$_2$ mass loading of 9.8 mg cm^{-2}.[30] It has been
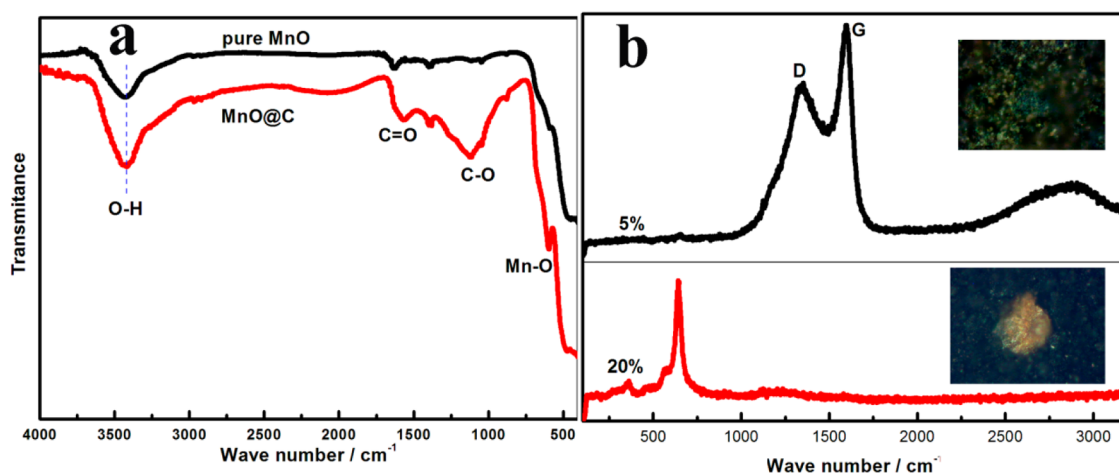
Figure 1. (a) FT-IR spectra of pure MnO and MnO@C and (b) Raman spectra of the MnO@C sample at different powers.

found that the low specific capacitance under high manganese loading densities is because only a thin surface layer of manganese oxide is involved in the charge storage process. In addition, the utilizability of active materials decreases with the increase in the loading of manganese oxide, which in turn results in a quick decrease in the redox activity of the manganese oxide and a significant degradation of capacitive performance.[31] Thus, a large phase contact area is essential for approaching a high electrochemical performance at a high mass loading density. However, the fabrication of such super-capacitor structure of MnO_2-based materials still remains a challenge.

In this paper, using a low-cost citric acid as carbon source, we synthesized a novel structure of MnO@C where MnO nanograins embedded in a carbon matrix. The inert MnO is then converted to birnessite-type MnO_2 with a unique sphere-like architecture by using galvanostatic charge−discharge technology. This electrode material shows a remarkably enhanced electrochemical performance characterized by a high specific capacitance, a good rate capability, and an extended cycling performance. The compact contact as well as the large phase contact area between the manganese oxide and the conductive carbon material led to high specific capacitance with high mass loading.

EXPERIMENTAL SECTION

Synthesis of MnO_2/C. The MnO_2/C composites were synthesized by the combination of liquid-phase precipitation reaction and a high temperature sintering method. Supporting Information Figure S1 shows the process for producing MnO_2/C compound. First, 1 mol KOH (Tianjin Kemiou) was dissolved into 200 mL distilled water and the solution was stirred with a magnetic stirrer at room temperature for 30 min. 200 mL of 0.5 mol L^{-1} $Mn(CH_3COOH)_2$ (Tianjin Kemiou) aqueous solution were then pumped into the above KOH solution to generate $Mn(OH)_2 \cdot xH_2O$ precipitates. The resulting powers were filtered, washed, dried at 80 °C for 12 h in air atmosphere, and thereafter mixed with citric acid (CA) at a mass ratio of 1:2 (Mn_3O_4: CA) for 24 h in a planetary dry ball mill. The XRD of dried product is shown in Supporting Information Figure S2. Subsequently, the mixture was heated in nitrogen at 700 °C for 6 h to produce MnO@C samples. Pure MnO were also synthesized with this method, but citric acid was not added. In order to obtained pristine carbon matrix, the MnO@C was etched in 1 M HCl aqueous solution to remove the embedded MnO cores.

The MnO@C electrodes were converted into birnessite MnO_2/C by the use of galvanostatic charge and discharge (NEWARE

autocycler) process at 0.5 A g^{-1} within potential window of −0.2 to 0.55 V vs Hg/HgO. The working electrodes were constituted of 80 wt % active material, 15 wt % acetylene black, and 5 wt % PTFE (60 wt % suspension in water). In order to approach a good contact, the viscous slurry was sandwiched by two nickel foams with an area of 1 cm × 1 cm, and the sandwich was pressed under a pressure of 10 MPa for 10 min. Then the electrode was dried under vacuum at 80 °C for 12 h. The mass loading of the active material is about 8 mg cm^{-2}. The counterelectrode was prepared from the mixture of activated carbon, acetylene black, and PTFE in a weight ratio of 80:15:5. The slurry was smeared onto a nickel foam of 2.5 cm × 2.5 cm in area. All the electrodes were immersed into a 6 mol L^{-1} KOH electrolyte solution. The cyclic voltammetry (CV) measurements were performed from −0.2 to 0.55 V at scanning rates of 5, 10, 20, 50, and 100 mV s^{-1}. The electrochemical impedance spectroscopy (EIS) was recorded over a frequency range of 0.01 to 100000 Hz with an AC modulation of 5 mV. Both CV and EIS were performed with a CHI 660E electrochemical workstation. All electrochemical experiments were carried out at room temperature.

Structure Characterization. The crystal structure of the samples was characterized by a Rigakud/MAX-2500/pc X-ray diffractometer with Cu Kα radiation, $\lambda = 1.54056$ Å. The field-emission scanning electron microscopy (FE-SEM) images and the energy dispersive spectroscopy (EDS) maps of as-synthesized products were measured with a scanning electron microscopy (SEM, S-4800, Hitachi, Japan, operated at 10 kV). The morphology and the microstructure of the samples were characterized by transmission electron microscope (TEM) and selected area electron diffraction (SAED) with a high resolution transmission electron microscopy (HR-TEM, JEM-2010). Raman spectra from 100 to 3200 cm^{-1} were recorded for the products by a Renishaw in via Raman microscope instrument, which is equipped with an Ar+ laser ($\lambda = 514.5$ nm), at ×50 magnification and powers of 5% and 20%. The thermal behavior of the precursors in nitrogen flow was analyzed by an in situ themogravimetric analyzer (TGA) (Pyris Diamond, PerkinElmer Thermal Analysis). The samples were heated from an ambient temperature to 800 °C at a heating rate of 10 °C min^{-1}. Fourier transform infrared spectroscopy (FTIR) analysis of the materials was performed on a Nicolet iS 10 Fourier transformation infrared spectrometer over a wavenumber range of 400 to 4000 cm^{-1}.

RESULTS AND DISCUSSION

Characterization of MnO and MnO@C. Figure 1a presents the FT-IR spectra of pure MnO and MnO@C. The peaks at 3442 cm^{-1} of both samples are attributed to the hydroxyl group and chemisorbed water. Compared with MnO, MnO@C exhibits a small peak centered at 1119 cm^{-1} and a broad peak centered at 1574 cm^{-1}, which are ascribed to the C−O group and C═O group, respectively.[32] This may testify

2192

dx.doi.org/10.1021/sc500379a | ACS Sustainable Chem. Eng. 2014, 2, 2191−2197

that oxygen acts as a special node to covalently bond Mn atom in MnO and carbon atom in carbon layer, which greatly improves the binding power of MnO with carbon.

Raman experiments present the chemical species in the surface region. Raman spectra of the MnO@C sample at different powers are shown in Figure 1b. Under a low power (5%), there are no sharp bands of manganese oxide over the spectra range, while the sharp and strong G band at 1594 cm^{-1}, compared to the weak D band at 1353 cm^{-1} (I_D/I_G = 0.9), confirms a high graphitization of the coated carbon layer. When the power increased to 20%, the bands for carbon disappeared. The bands in the ranges of 200−500 and 500−700 cm^{-1} are assigned to the Mn−O−Mn bending vibration and the Mn−O stretching of [MnO$_6$] octahedral, respectively.[32,33] This is attributed to the burning of carbon layer coming along with the oxidization reaction on the surface of the MnO under high energy laser. The insets of Figure 1b give a clear description of the burning of carbon.

To confirm the structure and to detect the carbon surrounding the MnO particles, the synthesized MnO@C powders were also examined by TEM. As shown in Supporting Information Figure S3a, the powders exhibit a solid grain shape and the MnO particles evenly distribute in a carbon network (inset of Figure S3a). The SAED image in Figure S3b indicates that MnO@C grains are of single crystal cubic phase. The close image to the carbon network (Figure S3c) confirms that the MnO is wrapped by a highly graphitic carbon, which is in good agreement with Raman observation. In order to characterize the structure of carbon networks, the nanoparticles were etched in 1 M HCl aqueous solution to remove the embedded MnO cores. It can be observed that carbon stacks on a grid and forms a 3D conductive carbon framework (Figure S3d). The porous texture of the sample with a pore size distribution in the range of 50−100 nm can be clearly identified in Figure S3e. Such a porous structure could be derived from the dissolution of MnO cores. This unique structure allows electrons effectively supply into the MnO cores through the solid thin carbon films during operation, leading to a rapid conversion of MnO to birnessite MnO$_2$.

The amount of the coated carbon was calculated based on the results of in situ TGA test (Supporting Information Figure S4). The mass loss of about 15% during heating from room temperature to 200 °C is due to the loss of water molecules existing both on the surface and in the materials. The weight loss in the temperature range of 200−500 °C results from the carbonization of citric acid. The inset of this figure is the TGA of pure MnO for comparison. The amount of carbon is calculated to be about 15%.

Conversion of MnO into Birnessite MnO$_2$. Figure 2a presents the XRD patterns of the samples before and after galvanostatic charge−discharge. All peaks of the MnO and MnO@C samples before cycling can be well indexed as cubic phase of MnO (JCPDS 06-0592). After 300 cycles, the intensities of the peaks of the pure MnO decreased (Figure 2a after cycling of MnO) and those of MnO@C sample (Figure 2a after cycling of MnO@C), corresponding to cubic phase, completely disappeared, while the peaks corresponding to the (002), (006), and (119) planes of birnessite-type MnO$_2$ (JCPDS 18-0802) appeared (Figure 2a after cycling of MnO@C and Figure 2b).

The surface morphology of MnO$_2$/C changes with galvanostatic charge−discharge cycling (Figure 3). The produced MnO@C initially is the grain particles with a
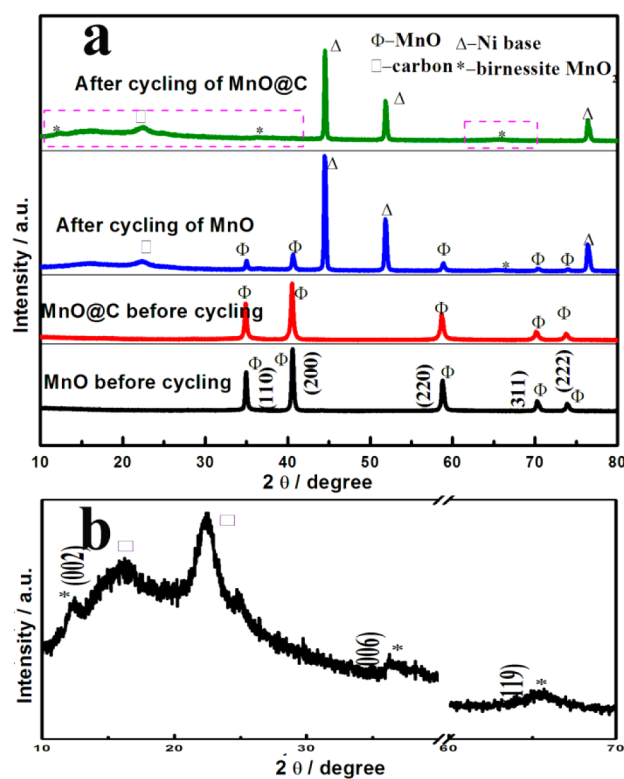

Figure 2. XRD patterns of (a) the samples before and after galvanostatic charge−discharge and (b) the segment parts marked with pink rectangles.

diameter of about 50 nm (Figure 3a and b). This grain morphology changes to flowerlike structure after 100 cycles (Figure 3c). The magnified image clearly depicts a flowerlike structure self-organized form ultrathin nanoflakes (Figure 3d). After 300 cycles, hierarchical porous microspheres with an average diameter of 1 μm are found (Figure 3e) in which the interconnected nanoflakes formed has a rippled surface superstructure. Figure 3f presents that microspheres with uniform ripple-shaped pores formed. These unique pores will provide channels for the diffusion of electrolyte ions into the interior of the materials and large surface areas for rapid surface redox reactions.

In order to further understand the structure of the MnO$_2$/C and the connection between MnO$_2$ and C, TEM was also carried out. Figure 4a clearly shows that the observed porous structure from the assembly of ultrathin flakes exists in the entire sphere. The inset of Figure 4a presents the diffraction pattern for a selected area of the circled diffraction spots within the rings reveal that the birnessite MnO$_2$ has a polycrystalline structure. After ultrasonic treatment, ripple-shaped nanoplates with black strip structure were found (Figure 4b). An interesting finding is that some carbon strips inlaid in the flake of MnO$_2$ and a well interpenetrative MnO$_2$−C composite was formed (Figure 4c), which will provide a high electron conductivity and mechanical reinforcement of the manganese oxides. For further validating the carbon-inlaid MnO$_2$ structure, EDS maps were measured, as shown in Figure 4d. The C−K signal was detected through the entire particle, indicating that the carbon is evenly distributed in the MnO$_2$ nanoplates.

As with the charge process, little Mn^{2+} dissolution on the surface of MnO grains occurs an electrochemical oxidation on the electrode surface, according to the following:
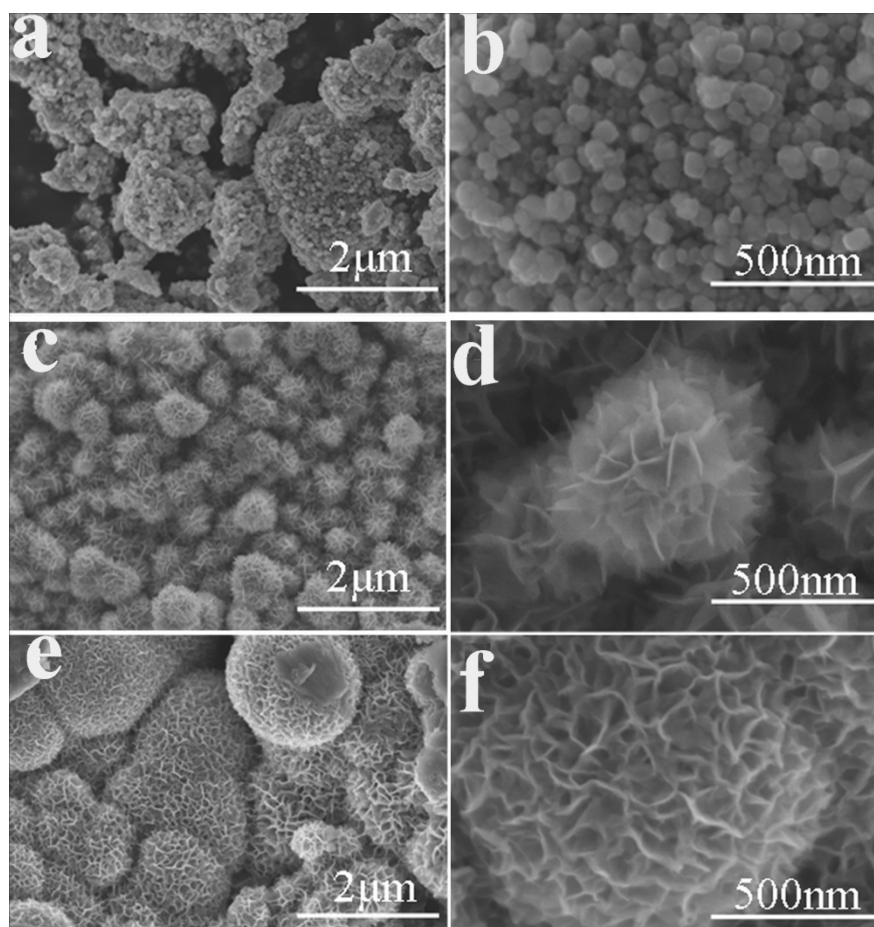
2193

dx.doi.org/10.1021/sc500379a | ACS Sustainable Chem. Eng. 2014, 2, 2191−2197

Figure 3. SEM images of (a, b) MnO@C matrix. (c, d) MnO@C after 100 cycles. (e, f) MnO@C after 300 cycles. Magnifications: (a, c, e) ×20 000 and (b, d, f) ×100 000.
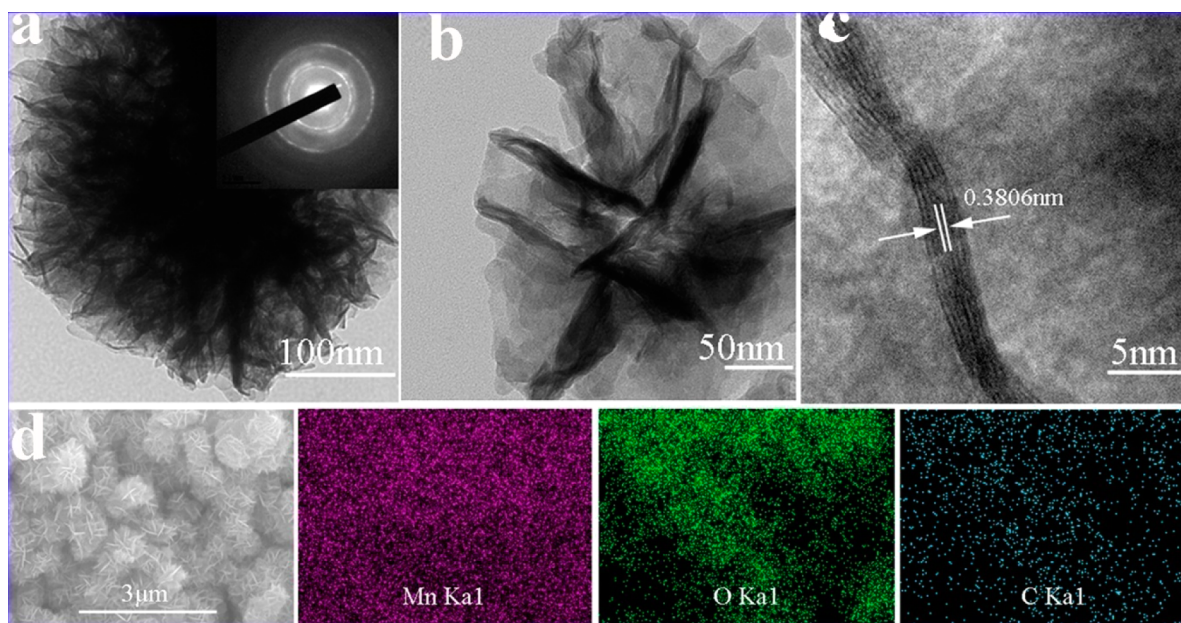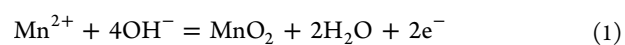

Figure 4. TEM image (after ultrasonic treatment) of (a, b) the birnessite-type MnO_2/C, (c) inlaid carbon strip, and (d) EDS maps of the synthesized MnO_2/C powders.

$$Mn^{2+} + 4OH^- = MnO_2 + 2H_2O + 2e^- \qquad (1)$$

Low nucleation rates result in few manganese oxides nuclei form during the initial stages of electrochemical oxidation. Subsequent epitaxial growth of thin nanosheets occurs on the
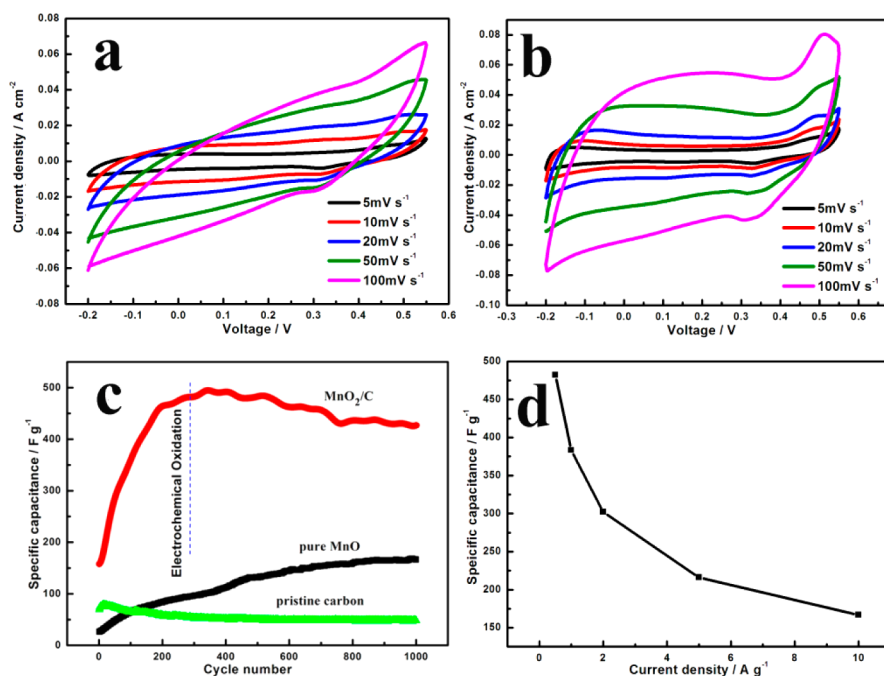
2194

dx.doi.org/10.1021/sc500379a | ACS Sustainable Chem. Eng. 2014, 2, 2191−2197

Figure 5. CV curves of (a) MnO after 300 cycles and (b) birnessite MnO_2/C at different scan rates. (c) Cycle performance of pure MnO, C, and MnO_2/C electrode at a rate of 0.5 A g^{-1}. (d) Rate performances of the MnO_2/C electrode performed in 6 M KOH solution vs Hg/HgO.

small radii oxide nanoparticles, leading to the formation of nanoflakes. Indeed, electrochemical oxidation process of MnO_2 from aqueous solution tends to form thin sheet-like deposits.[34] Based on thermodynamics, the surface energy of these individual nanoflakes is extremely high. To minimize the overall surface energy, the ultrathin flakes would tend to self-assemble to form a hierarchical architecture in the further reactions.[35,36] In the present work, under the galvanostatic charge−discharge process, the high conductivity carbon provided large sites for formation of nucleation and, subsequently, the nucleuses grew and formed a flake with a uniform flowerlike morphology. The formation of this curve structure may be also caused by the inner stress after carbon coating.

The pure MnO sample is composed of agglomerated irregular-shaped small grains (Supporting Information Figure S5a). When conducting cycling of up to 100 cycles, it is found that these small grains slightly convert into lamellar structure (Figure S5b). After 300 cycles, more grains on the surface of the electrode transformed to a sheetlike morphology (Figure S5c). It is also noticed that the thin sheets have a flat surface without pores.

As the analyses of the change of structure and surface morphology, carbon plays an important role on not only the crystalline phase transformation of the nanomaterial but also the morphological change of from nanoparticles to porous ball. During galvanostatic charge−discharge cycling, the carbon matrix provides large active sites for the transformation of manganese oxide, and the materials grow along these sites to form flowerlike structures quickly.

Capacitive Performances of Bitnessite-type MnO_2/C Composites. The performance of birnessite MnO_2/C (MnO@C after 300 cycles) is compared with that of MnO after 300 cycles at different scan rates (Figure 5a and b). Although the better symmetry character suggests that both have ideal capacitive behaviors, the higher specific current density of

the birnessite MnO_2/C than MnO at the same scanning rate indicates a superior specific capacitance of MnO_2/C.

Moreover, the birnessite MnO_2/C electrode remains a nearly symmetrical CV shape at scan rate as high as 100 mV s^{-1} (Figure 5b), which indicates an ideal capacitive behavior. This superior performance is closely related to its unique network structure. The galvanostatic discharge capacitance curve of the sample at current density of 0.5 A g^{-1} between the cutoff voltage −0.2 and 0.55 V is shown in Figure 5c and compared with pure MnO. A remarkable improvement can be clearly observed as inspecting the sharp increase in specific capacitance. Note that the specific capacitance of MnO_2/C (Figure 5c) increases to the highest value after 300 cycles, which probably relates to the electrochemical oxidation of MnO. MnO_2/C exhibited the highest mass-normalized specific capacitance, 485.6 F g^{-1}, and an area-normalized specific capacitance of 4.23 F cm^{-2} with a 88.9% capacitance retention after 1000 cycles. Whereas the pure MnO increased slowly and only 169 F g^{-1} was achieved after 1000 cycles. For comparison, the cycle performance of carbon matrix after removes the embedded MnO cores is also shown in Figure 5c. The specific capacitance of pristine carbon is much lower (50 F g^{-1}) than MnO_2/C, which indicated the contribution to capacitance from carbon is negligible. This result is well correspond with the data of XRD and SEM. Due to the rapidly changed of structure and surface morphology after carbon coating, MnO_2/C rapidly increased to the highest value. Figure 5d shows the discharge specific capacitance curves of the birnessite MnO_2/C at different current densities after cycling. The specific capacitance can remain 176 F g^{-1} as the current density increased to 10 A g^{-1}. The excellent performance of the MnO@C electrode can be ascribed to the synergistic effect from carbon and MnO_2. The highly graphitized carbon strips inlaying in the manganese oxides enhanced the electron conductivity and the mesoporous nature ensured the interaction between the electrolyte and the inner materials.
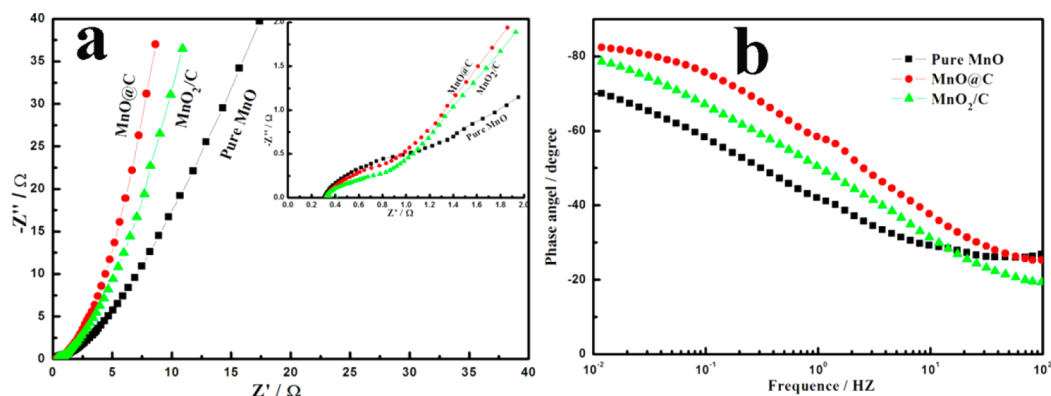
Figure 6. (a) Nyquist plots and (b) Bode plots of MnO, MnO@C, and MnO$_2$/C electrode in 6 M KOH electrolyte. (inset) Expanded high-frequency region of Nyquist plots.

In order to further investigate the electrochemical behavior of the produced samples, the impedance spectra of MnO, MnO@C and MnO$_2$/C (after cycling of MnO@C) were measured (Figure 6a). Compared to MnO, MnO@C has a depressed semicircle at high frequencies (inset of Figure 6a), which can be attributed to the small charge-transfer resistances between the electrode and the electrolyte. The low charge-transfer resistances may be caused by the high conductivity of carbon coated. It also can be seen that MnO$_2$/C also has a small charge-transfer resistances, indicating the high conductivity remains as before. Figure 6b shows the Bode plots of the three samples. At a certain phase angle, a high frequency indicates a faster ion response time. For carbon coating samples, the phase angle close to −90° at low frequencies represents a pronounced capacitive behavior with a small diffusion resistance.

CONCLUSIONS

A hierarchical porous birnessite-type MnO$_2$/C microsphere was synthesized by a high temperature solid state method and galvanostatic charge−discharge. It exhibits a high area normalized specific capacitance of 4.23 F cm^{-2} and a high specific capacitance of 485.6 F g^{-1} at the current density of 0.5 A g^{-1}. Moreover, this material possesses an excellent cycle stability, which remains 88.9% after 1000 cycles. This remarkably enhanced electrochemical performance is ascribed to the following structural features of the electrode: The mesoporous nature ensured the interaction between the electrolyte and the inner materials. The highly graphitized carbon strips dispersing in the manganese oxide formed an electric carbon network for enhancing the electron conductivity of birnessite-type MnO$_2$. The electric carbon network also strengthened the structure and accelerated the transfer of the low valence manganese oxide to an electrochemical active MnO$_2$, thereby, increased the electrochemical stability.

This work also revealed the important role of carbon in the structure change of birnessite MnO$_2$ and its pseudocapacitive performance. The carbon materials in manganese oxide exhibited their distinctive features for pseudocapacitors. Because of the excellent mechanical properties and superior conductivity, the carbon strips not only act as the active sites for the transformation of manganese oxide but also maintain the mechanical integrity and high electrical conductivity of the electrode materials. Thus, the electrochemical performance of the MnO$_2$/C remarkably increased.

ASSOCIATED CONTENT

ⓢ Supporting Information

SEM images of MnO@C, TEM images of pristine MnO, and the detailed material characterization results of TGA. This material is available free of charge via the Internet at http://pubs.acs.org/.

AUTHOR INFORMATION

Corresponding Authors

*Tel.: 0086-335-8061569. Fax: 0086-335-8059878. E-mail address: shaoguangjie@ysu.edu.cn (G.S.).
*E-mail: weimin.gao@deakin.edu.au (W.G.).

Notes

The authors declare no competing financial interest.

REFERENCES

(1) Toupin, M.; Brousse, T.; Belanger, D. Charge storage mechanism of MnO$_2$ electrode used in aqueous electrochemical capacitor. *Chem. Mater.* **2004**, *16*, 3184−3190.

(2) Sung, D. Y.; Kim, I. Y.; Kim, T. W.; Song, M. S.; Hwang, S. J. Room temperature synthesis routes to the 2D nanoplates and 1D nanowires/nanorods of manganese oxides with highly stable pseudocapacitance behaviors. *J. Phys. Chem. C* **2011**, *115*, 13171−13179.

(3) Duay, J.; Sherrill, S. A.; Gui, Z.; Gillette, E.; Lee, S. B. Self-limiting electrodeposition of hierarchical MnO2 and M(OH)$_2$/MnO$_2$ nano-fibril/nanowires: Mechanism and supercapacitor properties. *ACS Nano* **2013**, *7*, 1200−1214.

(4) Dong, R.; Ye, Q.; Kuang, L.; Wang, F. Enhanced supercapacitor performance of Mn$_3$O$_4$ nanocrystals by doping transition-metal ions. *ACS Appl. Mater. Interfaces* **2013**, *5*, 9508−9516.

(5) Chen, Q.; Meng, Y. N.; Hu, C. G. MnO$_2$-modified hierarchical grapheme fiber electrochemical super capacitor. *J. Power sources* **2014**, *247*, 32−39.

(6) Yan, J.; Khoo, E.; Sumboja, A.; Lee, P. S. Facile coating of manganese oxide on tin oxide nanowires with high-performance capacitive behavior. *ACS Nano* **2010**, *4*, 4247−4255.

(7) Jin, Y.; Chen, H.; Chen, M.; Liu, N.; Li, Q. Graphene-patched CNT/MnO$_2$ nanocomposite paper for the electrode of high-

2196

dx.doi.org/10.1021/sc500379a | *ACS Sustainable Chem. Eng.* 2014, 2, 2191−2197

performance flexible asymmetric supercapacitors. *ACS Appl. Mater. Interfaces* **2013**, *5*, 3408−3416.

(8) Wu, S.; Chen, W.; Yan, L. Fabrication of a 3D MnO$_2$/grapheme hydrogel for high-performance asymmetric supercapacitors. *J. Mater. Chem. A* **2014**, *2*, 2765−2772.

(9) Wu, M. S.; Guo, Z. S.; Jow, J. J. Highly regulated electro-deposition of needle-like manganese oxide nanofibers on carbon fiber fabric for electrochemical capacitors. *J. Phys. Chem. C* **2010**, *114*, 21861−21867.

(10) Lu, X. H.; Zhai, T.; Zhang, X. H.; Shen, Y. Q. WO$_{3-x}$@Au@MnO$_2$ core-shell nanowires on carbon fabric for high-performance flexible supercapacitor. *Adv. Mater.* **2012**, *24*, 938−944.

(11) Lang, X.; Hirata, A.; Fujita, T.; Chen, M. Nanoporous metal/oxide hybrid electrodes for electrochemical supercapacitors. *Nat. Nanotechnol.* **2011**, *6*, 232−236.

(12) Li, Q.; Wang, Z. L.; Li, G. R.; Guo, R.; Ding, L. X.; Tong, Y. X. Design and synthesis of MnO$_2$/Mn/MnO$_2$ sandwich-structured nanotube arrays with high supercapacitive performance for electro-chemical energy storage. *Nano Lett.* **2012**, *12*, 3803−3807.

(13) Chen, L. Y.; Kang, J. L.; Hou, Y.; Liu, P.; Fujita, T.; Hirata, A.; Chen, M. W. High-energy-density nonaqueous MnO$_2$@nanoporous gold based supercapacitors. *J. Mater. Chem. A* **2013**, *1*, 9202−9207.

(14) Hou, Y.; Chen, Y.; Hobson, T. Design and synthesis of hierarchical MnO$_2$ nanospheres/carbon nanotubes/conducting poly-mer ternary composite for high performance electrochemical electrode. J. Liu. *Nano Lett.* **2010**, *10*, 2727−2733.

(15) Han, J.; Li, L.; Fang, P.; Guo, R. Ultrathin MnO$_2$ nanorods on conducting polymer nanofibers as a new class of hierarchical nanostructures for high-performance supercapacitors. *J. Phys. Chem. C* **2012**, *116*, 15900−15907.

(16) Xiao, W.; Chen, J. S.; Lu, Q.; Lou, X. W. Porous spheres assembled from polythiophene(PTh)-coated ultrathin MnO$_2$ nano-sheets with enhanced Lithium storage capabilities. *J. Phys. Chem. C* **2010**, *114*, 12048−12051.

(17) Pang, H.; Deng, J.; Du, J.; Li, S. Porous nanocubic Mn$_3$O$_4$-Co$_3$O$_4$ composites and their application as electrochemical super-capacitors. *Dalton Trans.* **2012**, *41*, 10175−10181.

(18) Nagamuthu, S.; Vijayakumar, S.; Muralidharan, G. Synthesis of Mn3O4/amorphous carbon nanoparticles as electrode material for high performance supercapacitor applications. *Energy Fuels* **2013**, *27*, 3508−3515.

(19) Kim, J. H.; Lee, K. H.; Overzet, L. J.; Lee, G. S. Synthesis and electrochemical properties of spin-capable carbon nanotube sheet/MnO$_x$ composites for high-performance energy storage devices. *Nano Lett.* **2011**, *11*, 2611−2617.

(20) Ruiz, C. A.; Bélanger, D.; Rochefort, D. Electrochemical and spectroelectrochemical evidence of redox transitions involving protons in thin MnO$_2$ electrodes in protic ionic liquids. *J. Phys. Chem. C* **2013**, *117*, 20397−20405.

(21) Jiang, H.; Dai, Y. H.; Hu, Y. J.; Chen, W. N.; Li, C. Z. Nanostructureed ternary nanocomposite of rGO/CNTs/MnO$_2$ for high-rate supercapacitors. *ACS Sustainable Chem. Eng.* **2014**, *2*, 70−74.

(22) Sawangphruk, M.; Srimuk, P.; Chiochan, P.; Krittayavathananon, A.; Luanwuthi, S.; Limtrakul, J. High-performance supercapacitor of manganese oxide/reduced grapheme oxide nano-composite coated on flexible carbon fiber paper. *Carbon* **2013**, *60*, 109−116.

(23) Yu, M.; Zhai, T.; Lu, X.; Chen, X.; Tong, Y. Manganese dioxide nanorod arrays on carbon fabric for flexible solid-state supercapacitors. *J. Power Sources* **2013**, *239*, 64−71.

(24) Liu, M.; Gan, L.; Xiong, W.; Xu, Z.; Zhu, D.; Chen, L. Development of MnO$_2$/porous carbon microspheres with a partially graphitic structure for high performance supercapacitor electrodes. *J. Mater. Chem. A* **2014**, *2*, 2555−2562.

(25) Chen, H.; Zhou, S.; Wu, L. Porous nickel hydroxide-manganese dioxide-reduced grapheme oxide ternary hybrid spheres as excellent supercapacitor electrode materials. *ACS Appl. Mater. Interfaces* **2014**, DOI: 10.1021/am5014375.

(26) Xiao, Y.; Cao, Y.; Gong, Y.; Zhang, A.; Zhao, J.; Li, F. Electrolyte and composition effects on the performances of asymmetric supercapacitors constructed with Mn$_3$O$_4$ nanoparticles−graphene nanocomposites. *J. Power Sources* **2014**, *246*, 926−933.

(27) Zhao, Y.; Meng, Y.; Jiang, P. Carbon@MnO$_2$ core-shell nanospheres for flexible high-performance supercapacitor electrode materials. *J. Power Sources* **2014**, *259*, 219−226.

(28) Lei, Z. B.; Shi, F.; Lu, L. Incorporation of MnO$_2$-coated carbon nanotubes between grapheme sheets as supercapacitor electrode. *ACS Appl. Mater. Interfaces* **2012**, *4*, 1058−1064.

(29) Lei, Z. B.; Zhang, J.; Zhao, X. S. Ultrthin MnO$_2$ nanofibers on graphitic carbon spheres as high-performance asymmetric super-capacitor electrodes. *J. Mater. Chem.* **2012**, *22*, 153−160.

(30) He, Y.; Chen, W.; Li, X.; Zhang, Z. Freestanding three-dimensional grapheme/MnO$_2$ composite networks as ultralight and flexible supercapacitor electrodes. *ACS Nano* **2013**, *7*, 174−182.

(31) Jiang, H.; Yang, L. P.; Li, C. Z.; Yan, C.; Lee, P. S.; Ma, J. High-rate electrochemical capacitors from highly graphitic carbon-tipped manganese oxide/mesoporous carbon/manganese oxide hybrid nano-wires. *Energy Environ. Sci.* **2011**, *4*, 1813−1819.

(32) Ogata, A.; Komaba, S.; Baddourhadjean, R. Doping effects on structure and electrode performance of K-birnessite-type manganese dioxide for rechargeable lithium battery. *Electrochim. Acta* **2008**, *53*, 3084−3093.

(33) Sun, M.; Lan, B.; Yu, L. Manganese oxides with different crystalline structures: facile hydrothermal synthesis and catalytic activities. *Materials lett.* **2012**, *86*, 18−20.

(34) Wei, W.; Cui, X.; Mao, X.; Chen, W.; Ivey, D. G. Morphology evolution in anodically electrodeposited manganese oxide nanostruc-tures for electrochemical supercapacitor applications—Effect of supersaturation ratio. *Electrochim. Acta* **2011**, *56*, 1619−1628.

(35) Jiang, H.; Zhao, T.; Li, C. Z.; Ma, J. Hierarchical self-assembly of ultrathin nickel hydroxide nanoflakes for high-performance super-capacitors. *J. Mater. Chem.* **2011**, *21*, 3818−3823.

(36) Yan, J.; Fan, Z.; Sun, W.; Zhi, L.; Wei, F. Advanced asymmetric supercapacitors based on Ni(OH)$_2$ graphene and porous grapheme electrodes with high energy density. *Adv. Funct. Mater.* **2012**, *22*, 2632−2641.